

# A numerical analysis of unsteady inflow wind for site specific vertical axis wind turbine: A case study for Marsabit and Garissa in Kenya



David Wafula Wekesa<sup>a, b, \*</sup>, Cong Wang<sup>a</sup>, Yingjie Wei<sup>a</sup>, Joseph N. Kamau<sup>b</sup>,  
Louis Angelo M. Danao<sup>c</sup>

<sup>a</sup> Institute of Dynamics and Control of Spacecrafts, School of Astronautics, Harbin Institute of Technology, Harbin City, PR China

<sup>b</sup> Department of Physics, Jomo Kenyatta University of Agriculture & Technology, Nairobi City, Kenya

<sup>c</sup> Department of Mechanical Engineering, University of the Philippines, Diliman, Quezon City, Philippines

## ARTICLE INFO

### Article history:

Received 2 May 2014

Accepted 22 November 2014

Available online 12 December 2014

### Keywords:

Unsteady wind

VAWT

CFD

Wind energy potential

## ABSTRACT

Most of the wind analysis studies have been conducted under steady wind conditions. The study of real unsteady wind environment, however, is still an open-ended research question. This is attributable to the existing aerodynamic complexities under such conditions. In this paper, therefore, a numerical approach to investigate wind energy potential under unsteady conditions was proposed. In carrying out the study, the wind characteristics for two rural-urban towns in Kenya, namely Marsabit (2°19'N, 37°58'E) and Garissa (0°28'S, 39°38'E), were selected. A CFD analysis method was used to evaluate both unsteady wind inflow performance and the flow physics that affects the performance on a Vertical Axis Wind Turbine (VAWT). Using the validated CFD model, unsteady wind simulations were performed and the results obtained compared with empirical methods. Compared to the prevailing methods, the proposed numerical approach is not only computationally inexpensive, but also robust in both steady and unsteady wind conditions. The numerical method demonstrates that Garissa station is unsuitable for grid-connected power generation, while Marsabit station is suitable for both grid-connected and stand-alone power generation activities. The study results will hopefully be of importance to the wind industries that require designs for wind turbines reflecting real unsteady wind environment.

© 2014 Elsevier Ltd. All rights reserved.

## 1. Introduction

Wind energy is the latest alternative energy source that is renewable, and that has become an extremely popular field of research interest [1,2]. The wind converters, commonly referred as wind turbines, are classified as Horizontal Axis Wind Turbines (HAWTs) and Vertical Axis Wind Turbines (VAWTs) based on the rotor axis configuration with respect to the wind direction. Compared to the horizontal axis wind turbines, the vertical-axis wind turbines can be effectively used in urban areas where wind has characteristics of unsteadiness with turbulence [3]. Though VAWTs have inherent advantages in severe wind climates, HAWTs are dominant commercially as little research is available on VAWT aerodynamics. Yet, it has never been shown that the

HAWTs are fundamentally more aerodynamically efficient than the VAWTs [2,4].

The principal substantial advantages of the VAWTs are their ability to accept wind from any direction without yawing, typically quieter due to relatively lower rotational speed, ease maintenance and cheaper cost due to the location of the gearbox-generator system at the base of the turbine, as well as potentially better performance in unsteady and skewed wind conditions [2,5,6], and references therein]. The VAWT can be broadly divided into three basic types: Savonius type, Darrieus type, and Giromill type [4]. In the small-scale wind turbine market, the simple straight-bladed Darrieus VAWT is preferred due to its simple blade design.

The various methods used to investigate the performance of VAWTs can be categorized into numerical and experimental methods. The latter is limited by the huge capital cost requirements, an array of diverse technical skills, time constraints, operational know-how, and a number of physical and environmental parameters that can influence measurements [7]. Numerical methods can be classified into two types: The Computational

\* Corresponding author. Institute of Dynamics and Control of Spacecrafts, School of Astronautics, Harbin Institute of Technology, Harbin City, PR China. Tel.: +86 15734612395; +86 254 725037264.

E-mail addresses: [dwekesahit@gmail.com](mailto:dwekesahit@gmail.com), [david\\_@hit.edu.cn](mailto:david_@hit.edu.cn) (D.W. Wekesa).

Fluid Dynamics (CFD) methods that analyze directly the flow around the blade of a wind turbine; and the semi-empirical method of the Blade Element Momentum (BEM) theory that adopts the lift and drag coefficients of two-dimensional airfoils obtained by a wind tunnel test [8,9].

Although momentum theories have an advantage of a low computation effort, it is often difficult to investigate the complexity of aerodynamic phenomena involved in unsteady behavior of vertical axis turbines through theory of the blade elements [10,11]. The limitations by BEM theory can be overcome by CFD methods through the integration of the Navier Stokes equations in the neighborhood of the wind turbine blade profile [12].

Consul et al. [13], investigated solidity by use of a 2D CFD method to model a two-bladed and four-bladed VAWTs of NACA 0015 profile with corresponding solidities of  $\sigma = 0.019$  and  $\sigma = 0.038$ . Various tip speed ratios from  $\lambda = 3$  to  $\lambda = 8$  were analyzed to determine the effects of varying solidity on VAWT aerodynamic performance at steady inflow. From the study, the entire performance curve of the higher solidity VAWT is shifted to the left hence attaining the maximum power coefficient at  $\lambda = 4$ , while the smaller solidity VAWT attained maximum power coefficient at  $\lambda = 6$ . The shifting of the power performance curve to the left at higher solidity was attributed to the decrease in streamwise velocity presented with lower angles of attack.

A similar investigation was carried out in Ref. [14] to compare NACA 0012 and NACA 0022 profiles each of solidities  $\sigma = 0.2$ ,  $\sigma = 0.6$  and  $\sigma = 0.98$ . From the study, NACA 0012 performed better than the NACA 0022 for all tip speed ratios  $>3.5$ , while the performance of the NACA 0022 solidities was better at lower tip speed ratios than those of NACA 0012. In addition, the lower solidity turbines have a wider power coefficient-tip speed ratio (CP- $\lambda$ ) which reduces as the solidity (chord length) increases for both profiles. However, as in the study by Consul et al. [13], the choice of inlet free stream velocity was based on the steady wind speed tunnel experimental data that had been performed in Ref. [15]. Consequently, the realistic unsteady inflow wind experienced by vertical axis wind turbines operating in unsteady wind conditions was not considered.

Fully-coupled numerical modeling of offshore wind turbines using fully nonlinear CFD models for simplified models of wind turbines was studied by Viré et al. [16]. The work provides a first step towards the fully coupled simulations of floating wind turbines. However, the details of dynamics and aerodynamic performance for more complex and realistic wind turbine models were not considered as the study focus was on simplified models.

Castelli et al. [12], presented a numerical model to evaluate energy performance and aerodynamic forces acting on a straight-bladed vertical-axis Darrieus wind turbine using 2-D simulations of a classical NACA 0021 three bladed rotor. In this study, the 2D rotor was analyzed at 8 different tip speed ratios with a constant wind speed of 9 m/s. The work proved that CFD method was able to visualize the basic physics behind a VAWT, and that it can be used as an alternative to wind tunnel tests. There was a constant discrepancy of factor 2 between the numerical and wind tunnel experiments. This was associated with the effect of finite blade length and spoke drag that were not considered in the numerical analysis.

To yield and predict a higher performance, Castelli et al. [12] study was extended by Rosario et al. [17] using both open and novel vertical axis Augmented Wind Turbine (AWT) rotors. From this study, introduction of an augmented device (stator) around the rotor blades improved the power output of the VAWT by about 30%. The CP- $\lambda$  performance curve trend of the open rotor matched that by Castelli et al. [12], but with a higher CP of about 10%; a phenomenon which could be attributed to the difference in blade

profiles [17]. Similar to studies proposed in Refs. [13,14], simulations in both research were carried out under the assumption that the turbine was operating in steady and uniform wind conditions. Consequently, unsteady blade performance by turbine operating in unsteady wind conditions remained a challenge for this approach.

A parametric study by Saeidi et al. [18] indicated the need to provide site-specific small vertical axis wind turbines to evaluate their performance and derive important aerodynamic characteristics. In their study, a three bladed H-rotor VAWT was designed for nominal power production of 1.5 kWh for Fadashk station located in south of Khorasan province in Iran. To enable effective energy extraction, the study used the weather station wind characteristics data for the built environment to compliment the data from controlled wind tunnel conditions. However, like in the previous studies, the designed VAWT model using the BEM and double multiple stream tube model was based on steady inflow.

The aerodynamic performance of an isolated turbine within a steady inflow is not a representative of the actual performance of an operational urban wind turbine due to the inherent fluctuating wind [5]. Moreover, turbine performance is dependent on the cube of wind speed, hence moderate fluctuations in wind speed would result in very large fluctuation in available power. Therefore, for effective analysis of VAWT performance for a potential site, the energy contained within the frequency components of a fluctuating wind should be accounted for.

In Refs. [12–14,17,18], numerical and experimental investigation have been conducted on the performance of vertical-axis wind turbines using a steady inflow. Little work has been done on unsteady blade aerodynamic performance induced by unsteady wind conditions in the real urban environment. This is because turbine aerodynamics under varying wind conditions are still less understood. This is attributable to the current limitations of available computing power. In Refs. [19,20], the aerodynamic performance and wake dynamics have been investigated using a 2D free vortex model, both in steady and unsteady wind conditions of VAWTs. The authors limited their studies on low fluctuation frequencies within frequency range  $\leq 1$  Hz following McIntosh et al. [19] study that found the range to be a major part (over 90%) of the energy content.

The steady and unsteady wind conditions investigation of the aerodynamic performance and wake dynamics using vorticity transport model has been carried out by Scheurich et al. [21]. The unsteady wind conditions with a fluctuating mean wind speed of 5.4 m/s and a fluctuating frequency of 1 Hz was used. Out of the three blade configurations, helical blades performed much better than straight and curved blades, with the unsteady CP tracing the steady performance curve quite well. The results revealed that there is no significant increase in energy extraction at higher frequencies. That implies, there is no practical reason to extract the energy content at higher fluctuation frequencies. Furthermore, the numerical model results reveal a drop in performance at higher fluctuation amplitudes.

To further understand VAWT performance in unsteady wind conditions, Danao et al. [5] carried out an experimental investigation at a mean wind speed of 7 m/s. The experimental results of the study are the first of their kind, and provide a big break through in turbine aerodynamics research under varying wind conditions. For the mean wind speed of 7 m/s, the instantaneous CP rose and approached the steady CP profile of a higher free stream wind speed as the wind speed increased. Contrary to the works in Refs. [19–21], the unsteady VAWT performance did not follow the steady curves. However, the extent of the unsteady CP profiles was much shorter than that of the reference case when the fluctuation amplitude  $U_{amp}$  was reduced from  $\pm 12\%$  to  $\pm 7\%$ . Nevertheless, similar to works in Refs. [19–21], the unsteady free stream caused a drop in performance of the tested wind tunnel VAWT scale.

Through intensive CFD modeling, the aerodynamic performance and the flow physics surrounding VAWT blades in fluctuating winds were investigated by Danao et al. [22]. The presented results showed significant step forward in the understanding of VAWT performance in unsteady wind conditions. Danao et al. [22] extended the fluctuation frequency in Ref. [21] by considering fluctuation frequencies of 1 Hz and 2 Hz with a reference case of 0.5 Hz. The fluctuation amplitudes considered were  $U_{\text{amp}} = \pm 7\%$  and  $U_{\text{amp}} = \pm 30\%$  with a reference case of  $U_{\text{amp}} = \pm 12\%$ . A drop in performance was observed for large fluctuation amplitudes, while an increase in fluctuation frequency ( $>1$  Hz) was minor to the overall performance of a VAWT operating in periodically fluctuating wind conditions.

However, since Danao et al. [22] study was based on unsteady inflow wind conditions of wind tunnel scale with a mean speed of 7 m/s, analysis of actual wind energy potential of a vertical wind turbine operating in unsteady wind condition environment for specific sites was not considered. Therefore, there is need to extend the idealized assumptions used in Refs. [5,19–22] to actual wind speed fluctuations of VAWTs operating in unsteady wind conditions. In addition, generation of periodic fluctuations still remains a challenge in research due to the limitations in both numerical and wind tunnel experiments.

Wekesa et al. [23,24], carried out wind assessment and measurement study involving development of a high resolution data logging instrumentation system. This was to provide an efficient way for measuring wind speed and detecting wind direction for target sites. Using empirical methods, the wind resource potential for Eastern region of Kenya has been analyzed by Kamau et al. [26,27]. The results are very useful to the stake holders of wind technology including general wind evaluators. However, the empirical methods (including Power law and Weibull statistics) are not only limited in both time and cost, but they are also more prone to many statistical errors than numerical methods.

To overcome the limitations of empirical methods, we seek to investigate the wind performance of a VAWT under fluctuating wind speeds using a numerical method based on real wind characteristics of specific sites. We introduce a two-dimensional CFD method to analyze unsteady wind energy potential and power predictions of VAWTs operating in fluctuating winds. The wind characteristics for Marsabit ( $2^{\circ}19'N$ ,  $37^{\circ}58'E$ ) and Garissa ( $0^{\circ}28'S$ ,  $39^{\circ}38'E$ ) stations, both rural-urban towns in Eastern region of Kenya, have been selected as potential sites for the study. The results presented in this paper are significant to wind industries that require designs of wind turbines operating in unsteady wind environment at a specific potential hub site. In addition, the numerical approach provides detailed understanding of the VAWT aerodynamic performance in unsteady winds, and the flow physics that affects the performance.

## 2. Wind characteristics

In this study, a local set of wind data used were recorded at the standard height of 10 m by the Kenya Meteorological Department (KMD). A six year worth of wind data was available. An annual average wind speeds across six years were used as mean speed of unsteady wind  $U_{\text{mean}}$ , while annual mean standard deviations ( $\sigma_s$ ) averages, were used as the amplitude of fluctuation of unsteady wind,  $U_{\text{amp}}$  (see Equation (3)). From the empirical analysis in Refs. [26,27], the average annual wind speeds were 11.00 m/s and 3.42 m/s with standard deviations of 4.26 m/s and 2.60 m/s for Marsabit and Garissa stations, respectively. Summary of annual mean wind characteristics for the two station under study is as observed in Table 1.

**Table 1**  
Empirical wind characteristics.

Station	Average speed (m/s)	Std dev. ( $\sigma_s$ )	Weibull $k$	Weibull $c$ (m/s)	Power density (10 m)	Power density (50 m)	Wind class
Garissa	3.42	2.60	1.31	3.51	58	139	1
Marsabit	11.00	4.26	2.79	12.40	1038	2040	8

Wind speed distributions are necessary to quantify the available energy (power density) at a site prior to design of site specific wind turbine configurations [28]. Monthly or annual wind power  $P(v)$  per unit area  $A$ , for Marsabit and Garissa stations based on Weibull probability density function can be expressed as [26,29,30]:

$$\frac{P(v)}{A} = \frac{1}{2} \rho c^3 \left(1 + \frac{3}{k}\right), \quad (1)$$

where  $c$  (m/s) is the Weibull scale parameter,  $k$  is the dimensionless shape parameter, and  $v$  is the mean wind speed at the site. The Weibull dimensionless shape parameter  $k$  had a smaller spatial variation ranging between 1.26 and 1.38 than the scale parameter  $c$  which ranged between 2.92 m/s and 3.90 m/s for Garissa. For Marsabit station, the yearly values of  $k$  and  $c$  ranged from 2.05–3.05 and 11.86–12.96 m/s, respectively. The annual average wind speed for Garissa site was found to range from 2.5–3.5 m/s with an average of 3.42 m/s, while that of Marsabit ranged from 10.62–11.38 m/s with an average of 11.00 m/s as can be seen in Table 1. These are average wind speeds across the six years giving power densities of between 37 W/m<sup>2</sup> to 97 W/m<sup>2</sup> at 10 m for Garissa and 903–1119 W/m<sup>2</sup> for Marsabit [26,27].

The wind profile power law was used to relate the wind speeds at Meteorological standard height of 10 m and those at other heights. It is often used in wind power assessments where wind speed data at various heights must be adjusted to a standard height prior to use. The wind power law was used to convert the wind speed given by meteorological station at height of 10 m to the experimental heights. In order to ensure best energy yield, the urban wind turbines are mounted at higher heights to prevent the high roughness terrain effects [31]. The wind power law is expressed as

$$\frac{v_2}{v_1} = \left(\frac{h_2}{h_1}\right)^{\alpha}, \quad (2)$$

where  $v_2$  and  $v_1$  are the mean wind speed at heights  $h_2$  and  $h_1$ , respectively, while the exponent  $\alpha$  is an empirically derived coefficient related to roughness of the terrain which depends on surface topology and surrounding environment. The exponent value of 0.1429 has widely been chosen as a good representative of the prevailing conditions [26,27].

In our numerical model, the wind velocity fluctuations are idealized as sinusoidal with a mean value, an amplitude and a frequency. With respect to time, the instantaneous inlet velocity  $U(t)$  is:

$$U(t) = U_{\text{mean}} \pm U_{\text{amp}} \times \sin(2\pi ft), \quad (3)$$

where  $U_{\text{mean}}$  is the fluctuating mean wind speed,  $U_{\text{amp}}$  is the amplitude of fluctuation,  $f$  is the frequency of fluctuation, and  $t$  is the time.

### 3. Methodology

#### 3.1. Wind tunnel model

In Refs. [14,22,32], the 2D CFD model has been used to represent the virtual wind tunnel to reveal and predict the aerodynamic performance and flow physics around the VAWTs. Based on these studies, it has been shown that a 2D model is sufficient enough in predicting the performance and aerodynamics that surround the VAWT.

In this study, a steady wind performance is initially analyzed over tip speed ratio of range  $\lambda = 1.5$  to  $\lambda = 5$  in increments of 0.25 for constant free stream velocity,  $U_\infty$  of 11.00 m/s. This is the mean wind speed for Marsabit station, as can be observed in Table 1. The relative positions of the rotor blades and azimuth positions,  $\theta$ , with respect to the mid-chord of blade 1 are as shown in Fig. 1.

The CFD computational domain consists of two mesh zones; the inner circular Rotor sub-grid zone and the rectangular outer zone. The inner Rotor sub-grid zone is composed of three symmetric airfoil blades rotating at a common angular velocity. The three airfoil blades are spaced equally at  $120^\circ$  apart as shown in Fig. 1.

Fig. 2(a) shows the main wind tunnel scale dimensions and the boundary conditions of the 2D numerical wind tunnel domain. From the wall distance study by Danao et al. [22], the side wall distance was set to 1.2 m from VAWT axis giving a blockage ratio of 0.29 which is equal to that of the actual wind tunnel setup [5]. The rectangular outer domain is a wind tunnel grid with the wind velocity inlet boundary condition set to 1.8 m upwind with respect to the rotor test section similar to the actual wind tunnel setup that allowed the magnitude of inlet flow [5]. While, the pressure outlet boundary condition was set to 3 m downwind to match the actual distance of the wind tunnel fan from the VAWT axis of rotation [5]. According to Danao et al. [22], the downwind boundary study showed insignificant VAWT CP performance change over a wide range of tip speed ratios from 1.2 m to 3.0 m outlet distance with respect to the rotor axis. Hence, a 3.0 m boundary distance is sufficient. This was to ensure that the wake development by the VAWT was not terminated prematurely despite Danao et al. [22] revelation that no appreciable changes in torque was observed when the outlet boundary,  $d_0 \geq 2$  m from the VAWT axis. Moreover, there was no additional computational time due to the increase in outlet distance from the VAWT axis based on preliminary tests.

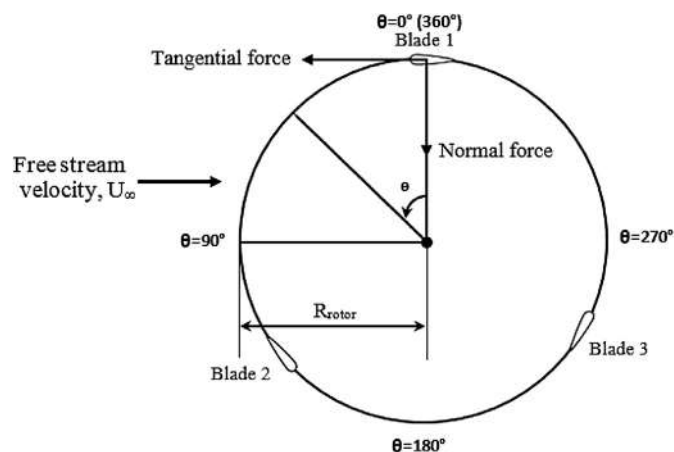
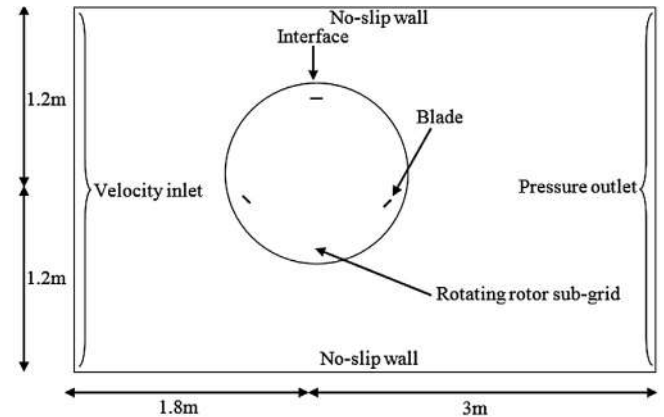
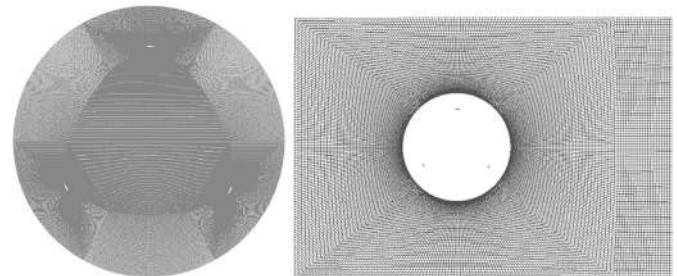


Fig. 1. Free stream wind direction, azimuth positions and orientation of blades [25].



(a) 2D numerical domain



(b) Rotating inner domain (c) Stationary outer domain mesh

Fig. 2. An illustration of the wind tunnel computational domain.

Therefore, the potential problem of computational boundaries interacting with the flow around the turbine was minimized. Since the main focus of the study is on VAWT unsteady inflow wind performance as a result of blade aerodynamic fluctuations, the computational boundary preliminary tests have not been discussed in this paper. The reader is referred to [22,33,34], and references therein] for full details on domain boundary location with both mesh and time step independence preliminary studies including the assumptions made.

The bottom and the top sides of the domain were defined as wall type boundary condition as was the case in studies by Danao et al. [5,22]. A symmetry type boundary condition was also tested, and results recorded were similar to the wall type boundary condition. Full 3D models were tested using course meshes but, were extremely expensive due to their immense computational time requirements; hence, were considered impractical and beyond the scope and aim of this study. Within the rectangular outer zone is a circular hole to fit in the inner circular Rotor sub-grid. The blades were defined as no slip walls, while both interface boundaries of the Rotor sub-grid and the outer rectangular wind tunnel sub-grid were set as an interface, thus ensuring the continuity in the flow field [36]. The interface was defined by coupling the stationary domain with the rotating one.

Following Wekesa et al. [25] CFD study on the influence of several parameters on unsteady wind performance of VAWTs, in this simulation, the effects due to rotor support arms and torque shaft were not taken into account due to the 2D simulation dimensionality. A moving mesh approach with a sliding mesh technique was used for the rotation of the inner circular Rotor sub-grid zone in order to capture the torque generated by the three blade airfoils. The 2D wind tunnel computational domain is as given in Fig. 2.

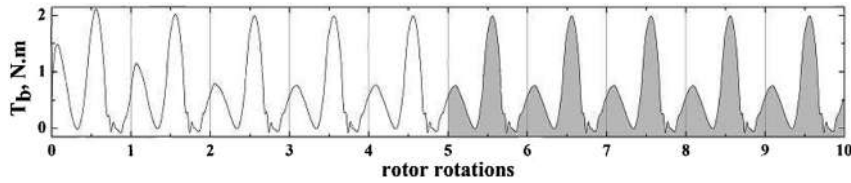


Fig. 3. 10 full rotations blade torque,  $T_b$ , ripple.

The inner circular Rotor sub-grid zone (see Fig. 2(b) coincides exactly with the circular opening within the outer stationary rectangular zone (see Fig. 2(c)). The interface of the two mesh zone boundaries slide against each other with no excessive overlap to minimize numerical diffusion, and have approximately the same characteristic cell size in order to obtain faster convergence [12,22]. The mesh was based on O-grid topology where the size of the first cell height next to the wall is limited by  $y^+ < 1$ . This was the limit of the turbulence model that was chosen for the simulations. The O-type mesh was primarily used in preference to conventional C-grid topology because the expected wake is not fixed on a specific path relative to the blade but rather varying greatly in direction swaying from one side to another side [22]. Using the mesh generation software ANSYS® ICFM CFD™, a structured mesh was employed for the computational domain, with the intention of reducing computational time [17].

The SIMPLE algorithm was used for coupling between pressure and velocity with a green-gauss cell based gradient evaluation option to solve Reynolds-Averaged Navier–Stokes (RANS) equations. The coupled pressure-based solver was selected with a second order implicit transient formulation for improved accuracy. All the solution variables were solved via second order upwind discretization scheme, since most of the flow can be assumed not to be in line with the mesh [22]. The under-relaxation factors used are the CFD package solver settings default values which are sufficiently large to avoid unconverged solutions that appear to be converged due to heavy under-relaxation. The turbulence intensity of inlet flow is set to 8% with a turbulence viscosity ratio of 14. These conditions were selected to provide a matching turbulence intensity decay that was observed in VAWT experiments conducted in the wind tunnel facility based on three NACA 0022 blades with chord  $c = 0.04$  m [5]. The rotor radius  $R_{\text{rotor}}$  and the blade span  $L$  are 0.35 m and

0.6 m, respectively, giving the VAWT a solidity of  $\sigma = 0.34$ . The solidity  $\sigma$ , can be expressed conventionally as [37]

$$\sigma = \frac{Nc}{R_{\text{rotor}}} \quad (4)$$

where  $N$  is the number of rotor blades.

### 3.2. Numerical set up

The simulation of flow over VAWT was studied by solving the unsteady RANS equations for the entire flow domain using commercial CFD software package ANSYS® Fluent®. This code uses the finite volume method to solve the governing equations for fluids. Applying Reynolds decomposition and taking time-average of the continuity and momentum equations yields the following unsteady RANS equations for incompressible flows [38–41]:

$$\frac{\partial u_i}{\partial x_i} = 0, \quad (5)$$

$$\frac{\partial u_i}{\partial t} + u_j \frac{\partial u_i}{\partial x_j} = -\frac{1}{\rho} \frac{\partial p}{\partial x_i} + \nu \frac{\partial^2 u_i}{\partial x_j \partial x_j} - \frac{\partial \overline{u'_i u'_j}}{\partial x_i}, \quad (6)$$

where,  $i, j = 1, 2$  whereas  $x_1$  and  $x_2$  denote the horizontal and vertical directions, respectively;  $u_i$  and  $u_j$  are the corresponding mean velocity components;  $t$  is the time;  $\rho$  is the density of the fluid;  $p$  is the dynamic pressure;  $\nu$  is the kinematic viscosity; and  $\overline{u'_i u'_j}$  is the Reynolds stress component where  $u'_i$  denotes the fluctuating part of the velocity. Detailed description about unsteady RANS approach formulation can be found in Refs. [36,38–44].

The CFD software package ANSYS® Fluent® which implements the unsteady RANS was used to directly obtain the instantaneous blade torque  $T_b$ . The obtained  $T_b$  was an average value after 9 rotations of the turbine assuring that the steady solution was reached. The irregularity in the torque peaks of upwind and downwind can be seen for the first five cycles as shown in Fig. 3. The blade torque peak values of the upwind and downwind for cycles 5 through to 10 matched closely; with a marginal difference of about 0.5% between the last five cycles of the rotation. This was a reflection of mesh quality, and time step size equivalent to  $1 \times 10^{-5}$  s for each physical time step. It was appropriate to select time step size at the lower tip speed ratio with converged solutions, so as to ensure convergence at the higher tip speed ratio was achieved [14,45].

A period corresponds to a revolution of  $120^\circ$  due to the three bladed rotor geometry; hence a  $360^\circ$  rotation was considered in all the simulations [25]. As can be seen in Fig. 3, a plot of  $T_b$  was monitored through 10 rotations; and a shift in the torque ripple for each succeeding blade by  $120^\circ$  is observed for rotations where the simulation is fully converged. Similar to a validation preliminary study in Ref. [25], at the last five cycles of rotation, each  $360^\circ$  torque ripple of one blade match the other blades at  $120^\circ$  apart. The time step convergence was monitored and the simulation was

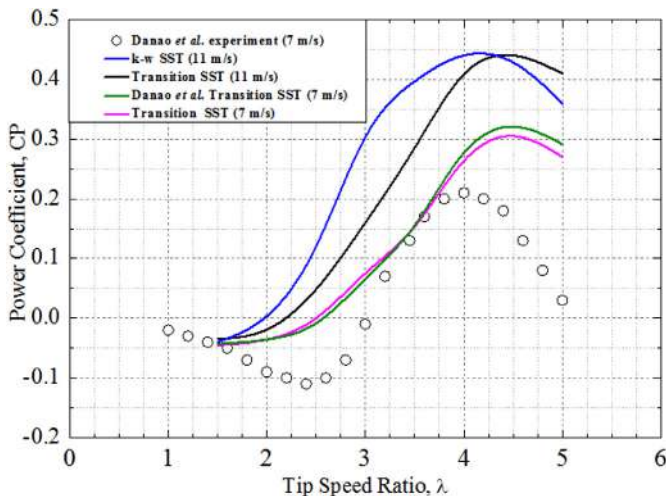


Fig. 4. Steady CP curves.

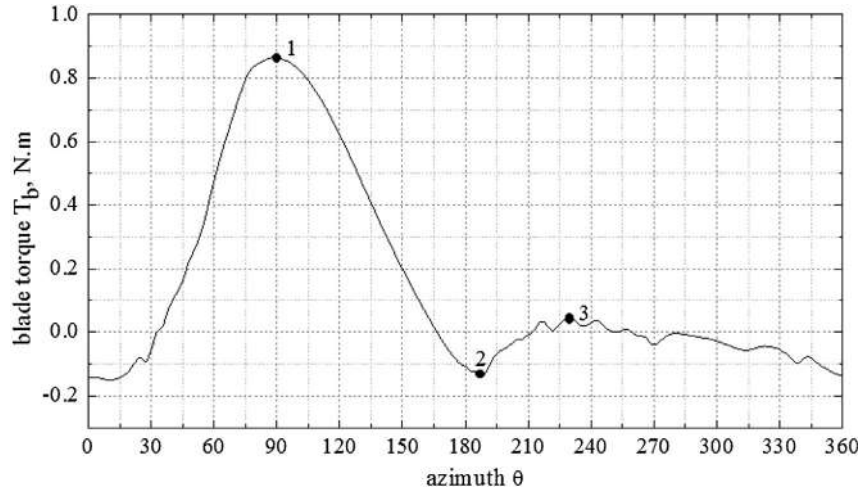


Fig. 5. Steady maximum blade torque for  $\lambda = 4.5$  at 11 m/s.

considered to have converged when residuals of all conserved variables fell below  $1 \times 10^{-5}$  [12,22,25].

The present simulations required an average of about 20 sub-iterations to make the solution converge at each physical time step. The simulations were performed on a single processor computer having, Intel® Core™ i7-2600 CPU@3.40 GHz clock frequency, 4 cores, 8 threads, physical RAM of 8 GB, and Windows 8 professional 64-bit operating system. A total Central Processing Unit (CPU) run time of about 3 days per data point of the steady CP curve was required which is approximately 42 days for each entire curve from  $\lambda = 1.5$  to  $\lambda = 5$  in both steady analyses. While, about 4 days total CPU run time were required for one unsteady wind condition simulation in both unsteady analyses under study.

### 3.3. Validation of CFD model

Appropriate CFD numerical validation solution has been conducted by Danao et al. [32] with a pitching airfoil experiment data at a Reynolds number of  $1.35 \times 10^5$ . According to the authors, the dynamic interactions of a pitching airfoil with a moving fluid give closest possible validation cases versus static airfoil data in the absence of VAWTs experimental data. The results show that both fully  $k-\omega$  Shear Stress Transport (SST) and the Transition SST were the most accurate models for predicting dynamic behavior compared to popular turbulence models like the one-equation Spalart-Allmaras (S-A) and the two-equation renormalization group RNG  $k-\epsilon$ . To assess the suitability of Danao et al. [32] results, Eboibi et al. [14] also revealed SST  $k-\omega$  model to be the most appropriate model that predicted the dynamic stall behavior from their Particle Image Velocimetry (PIV) experimental results.

Following blade kinematics and aerodynamics analyses in Wekesa et al. [25], from the moment coefficient equation (7), unlike lift and drag coefficients in equations (8) and (9), respectively, there is an additional factor  $R_{\text{rotor}}$  which is the rotor radius for VAWT. In both airfoil and VAWT applications, observe that equation (7) remains the same because we are getting the blade force coefficient and not the rotor coefficient. The only change is that in static airfoil studies, on the one hand coefficient of moment is normally computed about the quarter chord from the leading edge of the airfoil. On the other hand, for VAWT problems, moment coefficient is referred to from the VAWT rotation axis [25]. The moment coefficient  $C_m$  can be expressed as

$$C_m = \frac{T}{\frac{1}{2} \rho A R_{\text{rotor}} U_{\infty}^2}, \quad (7)$$

where  $T$  is the blade torque,  $A$  is the VAWT projected area,  $\rho$  is the fluid density,  $R_{\text{rotor}}$  is the rotor radius and  $U_{\infty}$  is the free stream wind velocity. The lift and drag coefficients can be expressed as

$$C_l = \frac{L}{\frac{1}{2} \rho A U_{\infty}^2}; \quad (8)$$

$$C_d = \frac{D}{\frac{1}{2} \rho A U_{\infty}^2}. \quad (9)$$

To check numerical models, and validate the fully turbulent  $k-\omega$  SST and Transition SST turbulence models, steady numerical simulations were carried out. The reference parameter for the present

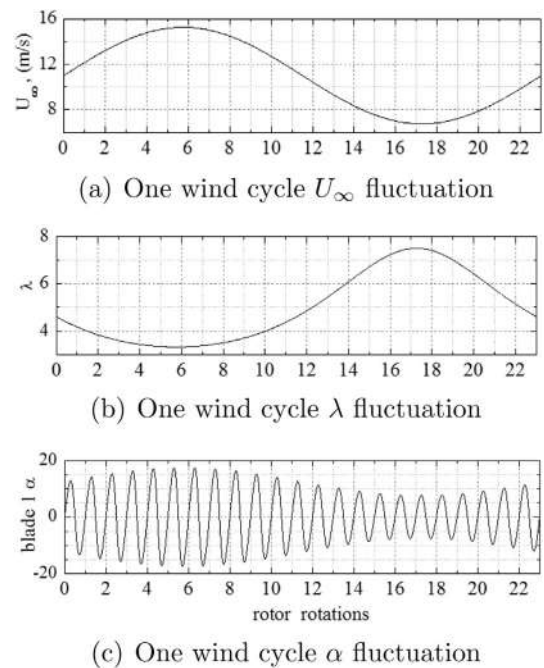


Fig. 6. One wind cycle variation of  $U_{\infty}$ ,  $\lambda$  and  $\alpha$  at  $U_{\text{mean}} = 11.00$  m/s.

analysis is the power coefficient (CP) plotted against the tip speed ratio ( $\lambda$ ) as the case in Refs. [22,25]. The tip speed ratio  $\lambda$ , is defined as the ratio between the circumferential velocity at the mid-span of the blade  $\omega R_{\text{rotor}}$ , and the free stream wind velocity  $U_{\infty}$ , expressed as [46]

$$\lambda = \frac{\omega R_{\text{rotor}}}{U_{\infty}} \quad (10)$$

where  $\omega$  is the rotational speed and  $R_{\text{rotor}}$  is the rotor radius.

The CFD simulations with a steady incoming winds of 11 m/s and 7 m/s were tested against the experimentally derived CP by Danao et al. [5] at different tip speed ratios from  $\lambda = 1.5$  to  $\lambda = 5$  in increments of 0.25. The incoming winds of 11 m/s and 7 m/s are free stream wind speeds  $U_{\infty}$  for Marsabit station (see Table 1) and Danao et al. [5,22], respectively. As can be seen from Fig. 4, both turbulent models over-predict the CP experiment starting from  $\lambda = 2.0$  to  $\lambda = 5$ . Two-dimensional VAWT models are essentially VAWTs with infinite blade aspect ratio AR which shifts the CP- $\lambda$  curve upwards and to the right as AR increases, but the general shape is maintained [17,22,35].

As can be seen in Fig. 4, the maximum CP for the experiment is 0.21 at  $\lambda = 4.0$ , while the study's Transition SST model maximum CP is 0.30 at  $\lambda = 4.5$  for steady speed of 7 m/s. The study's Transition SST results are similar to those of Danao et al. Transition SST model [22], maximum CP of 0.33, at a 7 m/s. The marginal over prediction by 0.03 at  $\lambda$  range of 3.5–5 in Danao et al. [22] could be attributed to the differences in the outlet and inlet distances by 1 m and 0.3 m, short of the 3 m and 1.8 m, respectively, to the study's wind tunnel domain (see Fig. 2(a)). That means, the effect of developed wake was minimized to match wind tunnel set up conditions [5,25]. However, at low  $\lambda$  of between 2 and 3.5, the reverse marginal difference was observed in CP. This could be the result of the presence of the centre post in Danao et al. [22] model that generates a wake; hence, leading to blade interaction. The results are similar to a CFD model validation solution in Ref. [25].

At 11 m/s, the maximum CP is 0.45 at  $\lambda = 4.0$  for fully turbulent while CP is 0.45 at  $\lambda = 4.5$  for Transition SST model. In addition, it can be observed in Fig. 4, that the Transition SST generates maximum CP at  $\lambda = 4.5$  for both wind speeds, with  $U_{\infty} = 11$  m/s predicting higher CP and wider band of positive performance than  $U_{\infty} = 7$  m/s. The higher CP over-prediction at 11 m/s was expected

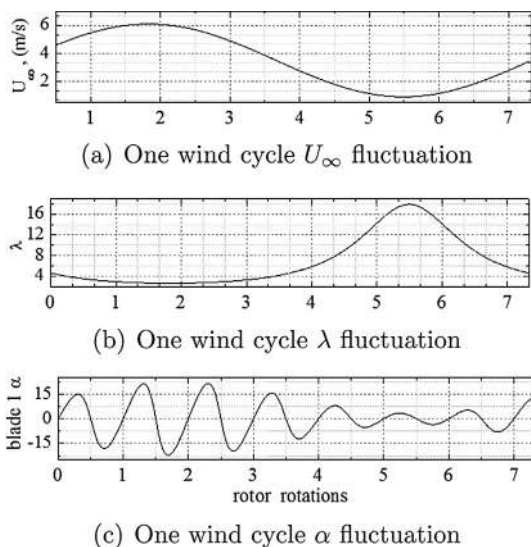


Fig. 7. One wind cycle variation of  $U_{\infty}$ ,  $\lambda$  and  $\alpha$  at  $U_{\text{mean}} = 3.42$  m/s.

as a result of wind power dependency on the cube of the wind speed as expressed in equation (12). The results are consistent with published work in Refs. [2,12,22,25,33,47], where 2D power coefficients were over-predicted over the entire range  $\lambda$ . The CP over prediction could be as a result of 2D model inability to account for finite blade span as well as the blade-support arm junction effects and support arm drag that are present in the actual setup [12,48]. The fully turbulent  $k-\omega$  SST predicts delayed blade stall which prolongs positive torque generation. This leads to higher CP performance within low tip speed ratio versus the transition SST model as can be seen in Fig. 4 at 11 m/s.

As shown in Fig. 4, the Transition SST model is closer and in good agreement with experimental results for positive performance prediction compared to the fully turbulent SST model. Therefore, in this study, we have chosen the Transition SST model as the one appropriate for our VAWT simulations.

The entire picture of a single blade torque ripple as it goes around one full rotation for  $\lambda = 4.5$  at 11 m/s (with maximum CP of 4.5) is given in Fig. 5. It can be observed that the maximum  $T_b$  occurs at  $\theta = 90^\circ$  (Point 1.) After this region, the  $T_b$  rapidly drops, and reaches the negative region as the blade exhibits stalled flow at  $\theta = 189^\circ$  (Point 2). The downwind maximum  $T_b = 0.04$  Nm occurs at  $\theta = 22^\circ$  (Point 3.) The difference in maximum  $T_b$  value at point 1 and 3 was expected due to power extraction in the upwind that subsequently lowers the available energy content in the flow. Since the study's main focus is on unsteady wind inflow investigation, in unsteady wind conditions, detailed explanation for steady aerodynamic performance as the blade completes a rotation at  $\theta = 360^\circ$  can be obtained in [12,32,34,49].

## 4. Results and discussion

### 4.1. Unsteady inflow wind performance

The optimized numerical model developed for the steady wind case is used in the unsteady wind simulations. Apart from the unsteady wind inflow at the velocity inlet boundary condition, the only other distinction regarding the unsteady wind model, is that all three blades are monitored as opposed to one blade force monitor in the steady wind case [22].

Based on commercial scale models for unsteady winds in [20,21,50] and wind tunnel scale models by Danao et al. [5,22], it was estimated that the highest frequency with meaningful energy content in unsteady wind environment with fluctuating wind conditions is within frequency range  $\leq 1$  Hz. The authors assert

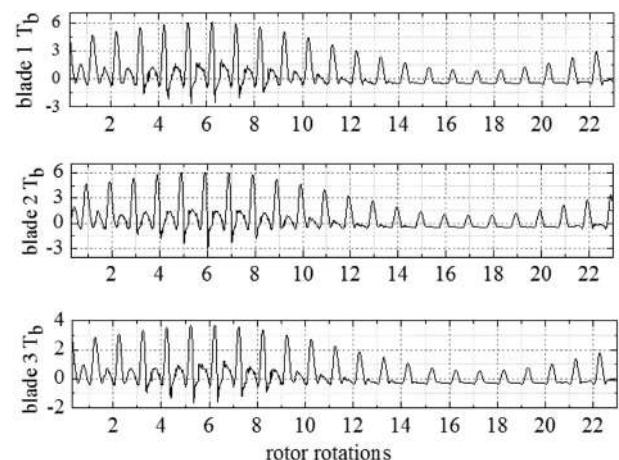


Fig. 8. Blade  $T_b$  variations across the three blades at  $U_{\text{mean}} = 11.00$  m/s.

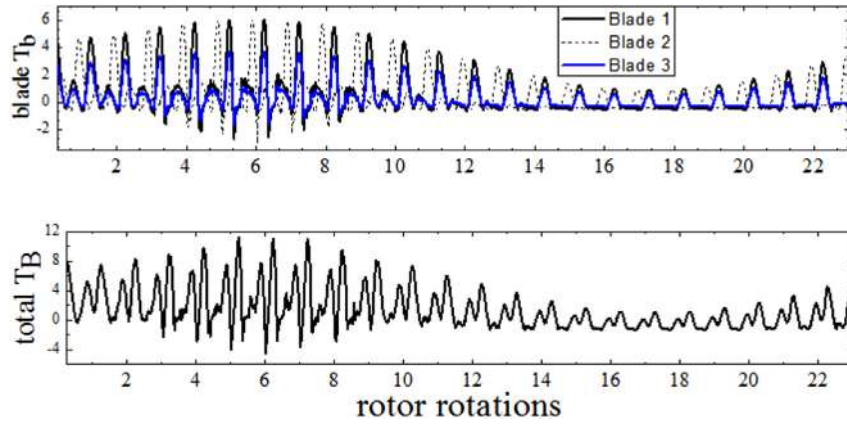


Fig. 9.  $T_b$  and  $T_B$  variations at  $U_{\text{mean}} = 11.00$  m/s.

that, this corresponds to operating conditions that most turbines would likely encounter in unsteady wind environment. That implies, there is no practical reason to extract the energy content at higher fluctuation frequencies.

Therefore, in the present work, all simulations have been conducted at fluctuation frequencies within this range. The power performance behavior of the VAWT model is compared in both two wind conditions with a common fluctuating frequency and tip speed ratio.

#### 4.2. Unsteady inflow wind fluctuations

The wind conditions for Marsabit and Garissa stations are used as the baseline for which the VAWT model analysis is done. As alluded to earlier (refer to Equation (3)), and as can be seen from the wind data in Table 1, the mean speed of unsteady wind at Marsabit station is  $U_{\text{mean}} = 11.00$  m/s with fluctuation amplitude of  $U_{\text{amp}} = \pm 39\%$  ( $\pm 4.26$  m/s), while at Garrisa station is  $U_{\text{mean}} = 3.42$  m/s with  $U_{\text{amp}} = \pm 76\%$  ( $\pm 2.60$  m/s). A common fluctuation frequency  $f_c = 1$  Hz is used for both simulations. The rotor angular speeds are constants  $\omega = 145$  rad/s (1385 rpm) and  $\omega = 45$  rad/s (427 rpm) for Marsabit and Garissa stations, respectively, both resulting in a mean tip speed ratio  $\lambda_{\text{mean}} = 4.6$ . The mean tip speed ratio  $\lambda_{\text{mean}} = 4.6$  is just above the maximum peak CP of the steady tip speed ratio  $\lambda^* = 4.5$ . This way, any fluctuation was to avoid low tip speed ratios to the left of peak CP which are unstable region of operation [22,50].

Following McIntosh et al. [20] and Wekesa et al. [25] notations for VAWT experiencing a gust, the number of rotor rotations  $n_{\text{rev}}$ , in one full cycle of the wind fluctuation can be expressed as [25]:

$$n_{\text{rev}} = \frac{\lambda_{\text{mean}} U_{\text{mean}}}{2\pi R_{\text{rotor}} f_c} \quad (11)$$

where  $\lambda_{\text{mean}}$  is the mean tip speed ratio defined as  $\lambda_{\text{mean}} = \omega_{\text{mean}} R_{\text{rotor}} / U_{\text{mean}}$ ,  $U_{\text{mean}}$  is the fluctuating mean wind speed,  $R_{\text{rotor}}$  is the rotor radius and  $f_c$  characteristic fluctuation frequency. Therefore, in the present wind conditions, 23 and 7.5 full rotations of the rotor were allowed to run to capture periodic convergence each associated with one wind cycle for fluctuating mean wind speeds  $U_{\text{mean}}$  at 11.00 m/s and 3.42 m/s, respectively.

Observe in Fig. 6(a) that, a simple sine wave profile for  $U_{\text{mean}} = 11.00$  m/s fluctuations is assumed, and the simulation is such that one wind cycle is exactly 23 rotor cycles. That means a total of 23 rotor rotations completes one periodic wind cycle. Nevertheless, the simulations had to be run for 30 full rotations of

the VAWT in order to have a data set that is sufficiently long to cover 23 full rotations in an entire wind cycle.

From Equation (10), we may conclude that an increase in  $U_{\infty}$  results in a decrease in  $\lambda$  due to their inverse relationship at constant rotational speed  $\omega$ . The incoming  $U_{\infty}$ , increases from its mean value of 11.00 m/s to the upper peak value of 15.26 m/s at the end of the 5th rotation; just before the 6th rotation, with  $\lambda$  dropping to a minimum value of 2.32; close to the point of maximum wind speed (Fig. 6(a)). At this point, the effective maximum  $\alpha$  generated is 17.5. The  $U_{\infty}$  then drops back in speed to the mean wind speed as the blade passes the 180° azimuth position. The wind speed continues to fall until it reaches the lowest trough value of 6.74 m/s (at the 17th rotation). After which it rises again in mean velocity as the blade completes one wind cycle. At minimum  $U_{\infty}$ ,  $\lambda$  rises to its maximum value of 7.51 before finally dropping back to initial  $\lambda_{\text{mean}} = 4.6$  (Fig. 6(b)). Observe in Fig. 6(c) that, a low  $\alpha$  of 7.6° is generated by blade 1 at minimum  $U_{\infty}$ .

Contrary to the observation in Fig. 6(a), the sinusoidal wave profile of the fluctuating wind at  $U_{\text{mean}} = 3.42$  m/s is distorted as shown in Fig. 7(a). Similar to the wind conditions for  $U_{\text{mean}}$  of 11.00 m/s, a fluctuation frequency of  $f_c = 1$  Hz has been used. A constant rotor angular speed  $\omega$  of 45 rad/s (427 rpm) is applied to provide an initial  $\lambda_{\text{mean}}$  of 4.6 (see Fig. 7(b)). From Fig. 7(a), it can be observed that the wind speed fluctuates to a positive peak of 6.02 m/s while  $\lambda_{\text{mean}}$  drops to 2.62, almost at the same point as that of positive wind speed peak. This confirms the unsteady  $\lambda$

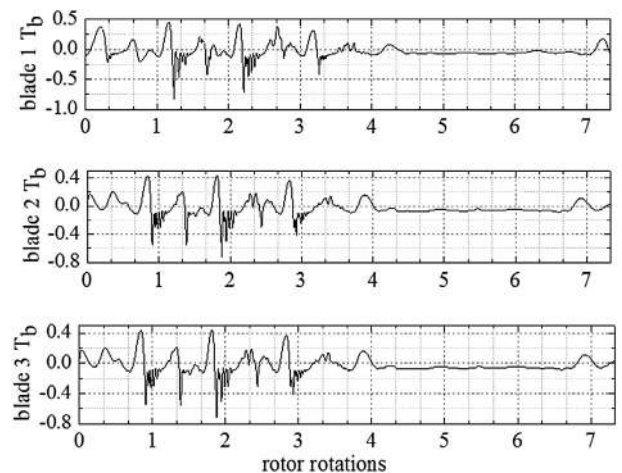


Fig. 10. Blade  $T_b$  variations across the three blades at  $U_{\text{mean}} = 3.42$  m/s.

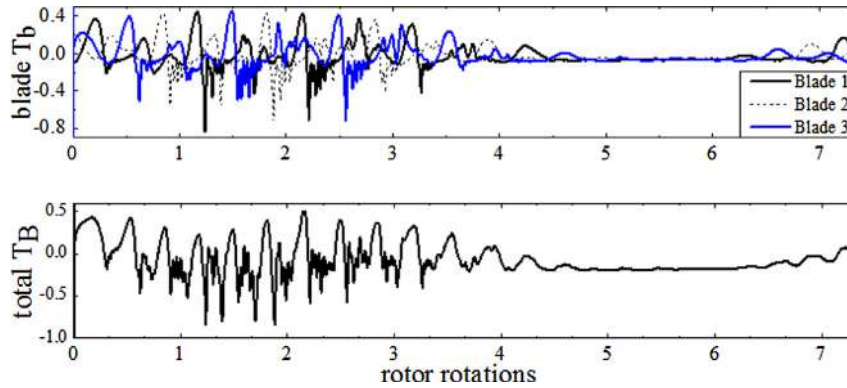


Fig. 11.  $T_b$  and  $T_B$  variations at  $U_{\text{mean}} = 3.42$  m/s.

instantaneous relationship between  $\omega$  and  $U_\infty$  (refer to Equation (10)) of which  $\lambda$  is more sensitive to fluctuating wind speed as opposed to rotor angular speed. Beyond positive  $U_\infty$  peak, the wind speed drops to the lowest magnitude of 0.82 m/s as  $\lambda$  attains its positive peak value of 19.21 close to the point of minimum wind speed. At this point, as can be observed in Fig. 7(c), a low  $\alpha$  is generated by the blade. Therefore, from Figs. 6 and 7, maximum  $\alpha$  increases with increasing  $U_\infty$ ; and VAWT runs at a constant angular velocity  $\omega$  due to its inertia despite the fluctuating wind conditions.

#### 4.3. Power performance

In this study, the cycle-averaged power coefficient CP of a turbine operating in an unsteady wind can be defined as the blade average power  $P_B$  over wind average power  $P_w$  expressed as [25],

$$CP = \frac{P_B}{P_w} = \frac{T_B \omega}{\frac{1}{2} \rho A U_\infty^3} \quad (12)$$

where  $\omega$  is the rotor angular speed,  $U_\infty$  is the free stream wind velocity, and  $T_B$  is the total blade torque, which is the average of the instantaneous torque of the three blades obtained by the solver (see Equation (7)). The blade average power is computed by computing the average of the instantaneous blade power of the three blades over the entire wind cycle [25].

Fig. 8 shows the variation of blade  $T_b$  across the three blades for  $U_{\text{mean}} = 11.00$  m/s. The plots of  $T_b$  for the three blades in one full cycle of the fluctuating wind are monitored. The shape of the  $T_b$

profile for both blades widens with increasing  $\lambda$  (see Fig. 6(b)). This is attributable to very low stall and shallow flow separation resulting from low  $\alpha$  at the region. Therefore, the blades generate very low but slightly prolonged torques as they pass the second half of the wind cycle.

The maximum peak  $T_b$  values for all blades increases together with increasing fluctuating speed  $U_\infty$ . In addition, unlike the steady case, the blade torque profile is not the same for all blades. This is because, at each instant time, each blade experiences different wind speeds as a result of unsteady inflow. The maximum  $T_b$  values are 6.06 Nm, 6.05 Nm and 3.71 Nm for blades 1, 2, and 3, respectively, all generated within the 6th rotation (refer to Fig. 8).

The combined maximum blade torque  $T_B$  is 11.18 Nm, generated within the 5th rotation (see Fig. 9). This can be as a result of relatively small negative  $T_b$  fluctuations experienced by the blades within the 5th rotation rather than in 6th rotation. The peak  $T_b$  performance falls to 0.88 Nm, 0.87 Nm and 0.54 Nm at a point of extreme  $U_\infty$  value in the second half of the wind cycle for blades 1, 2, and 3, respectively, all within the 17th rotation (see Fig. 8).

Therefore, at each instant time each blade registers different torques. This is attributable to the variation in both direction and magnitudes of the wind velocity that each blade achieves at instant time. From Fig. 9, we may conclude that the total  $T_B$  of the entire wind cycle is generally positive and plummets down to 0.99 Nm, also within the 17th rotation. However, in spite of the unsteady wind characteristics at the station, a positive overall torque performance is generated over the entire fluctuating wind cycle.

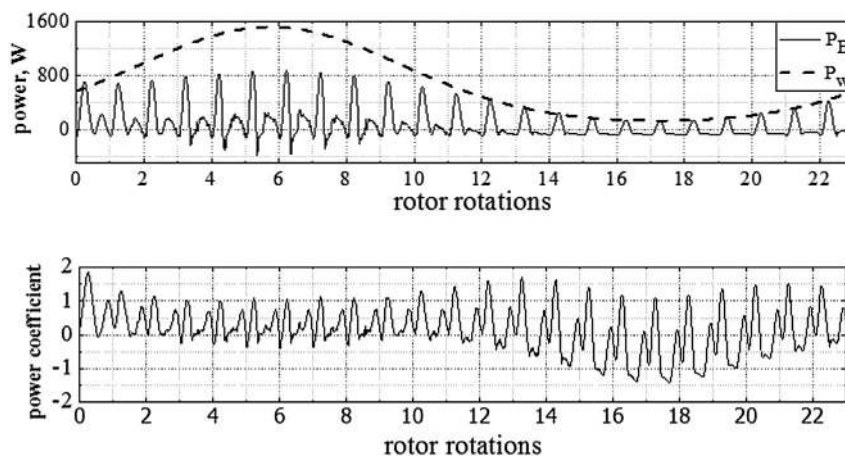


Fig. 12. One wind cycle  $P_B$ ,  $P_w$  and CP variations at  $U_{\text{mean}} = 11.00$  m/s.

**Table 2**  
Numerical power performance.

Station	$U_{\text{mean}}$ (m/s)	$U_{\text{amp}}$ (m/s)	CP		$P_B$ (W)	$P_w$ (W)
			CP <sub>steady</sub>	CP <sub>unsteady</sub>		
Marsabit	11.00	4.26	0.45	0.30	204.86	698.43
Garissa	3.42	2.60	-0.05	-0.13	-4.30	33.59

In Fig. 10, we observe that the  $T_b$  variations at  $U_{\text{mean}} = 3.42$  m/s across the three blades is negative as compared to the wind condition at  $U_{\text{mean}} = 11.00$  m/s. As shown in Fig. 8, the plots of  $T_b$  for the three blades in one full wind cycle also display different torques (see Fig. 10). The maximum peak  $T_b$  values for all blades increases together with increasing fluctuating speed  $U_{\infty}$ , but performing in a negative region over the entire wind cycle. The maximum peaks are both generated within the 1st and 2nd rotation. A relatively low maximum  $T_b$  value of 0.43 Nm is generated by both blades within the 2nd rotation.

From Fig. 11, negative torque performance is registered as the  $\lambda$  increases (see Fig. 7(b)) with an extreme minimum value of  $-0.08$  Nm from the 4th rotation all the way to the end of the wind cycle. The total maximum blade torque  $T_B$  is 0.5 Nm, also generated within the 2th rotation as can be seen in Fig. 11. From Figs. 9 and 11, the total maximum  $T_B$  drops from 11.18 Nm at  $U_{\text{mean}} = 11.00$  m/s to 0.5 Nm at  $U_{\text{mean}} = 3.42$  m/s, both occurring at the quarter cycle region of the wind cycle. The large drop in torque performance of VAWT model is due to relatively higher  $U_{\text{amp}}$  of  $\pm 76\%$  ( $\pm 2.60$  m/s) at Garissa station as compared to 39% ( $\pm 4.26$  m/s) at Marsabit station.

Fig. 12 shows the variation of rotor power  $P_B$  and fluctuating wind power  $P_w$  across the wind cycle for  $U_{\text{mean}} = 11.00$  m/s. The available power in the wind increases with rising free stream velocity  $U_{\infty}$  up to the maximum peak values generated within the 6th rotation. The  $P_B$  and  $P_w$  profiles follow the total torque  $T_B$  profile (see Fig. 9). The maximum peaks for  $P_B$  and  $P_w$  are 875 W and 1524 W, respectively. Afterwards, wind power plummets to its minimum value of 131 W as  $U_{\infty}$  drops to lowest value of 6.74 m/s in the second half of the wind cycle.

As shown in Fig. 12, the available wind power increases from  $P_w = 570.67$  W to a peak value of  $P_w = 1523.59$  W at maximum  $U_{\infty}$  of 15.26 m/s, while at minimum  $U_{\infty} = 6.74$  m/s, minimum  $P_w$  of 131.13 W is obtained. This was expected because the power in the wind is a function of the cube of the wind velocity as expressed in Equation (12). Similar to a previous study in Ref. [25], from Fig. 6(a,b) and 12, we may conclude that the performance of the

turbine in a fluctuating wind is a function of the tip speed ratio set by its controller, and follows the wind velocity variations.

From Table 2, it can be seen that  $P_w$  and  $P_B$  cycle averages at Marsabit station are 698.43 W and 204.86 W, respectively. The corresponding cycle averaged CP is 0.30; a drop of about 35% from the steady maximum CP of 0.45 at  $\lambda^* = 4.5$  (see Fig. 4). The actual amount of blade power generated is less than available wind power since not all the available wind is extractable.

Fig. 13 shows the plot of variation of power and cycle-averaged CP over the wind cycle at  $U_{\text{mean}} = 3.42$  m/s. At this wind condition, the cycle-averaged  $P_B$  is  $-4.30$  W, while the  $P_w$  is 33.59 W, generating cycle-averaged CP close to zero of  $-0.13$  as shown in Table 2. This is a deterioration in performance of about 160% drop from the steady CP maximum of  $-0.05$  at  $\lambda^* = 0.45$ . As can be seen in Fig. 13, the cycle-averaged CP is zero for the entire first half cycle. The second half cycle is the worst performing with a cycle-averaged CP of  $-27.7$ , generated at the mid of the 5th rotor cycle. At this point, wind and blade powers are 0.29 W and  $-7.99$  W, respectively, while the  $U_{\infty}$  falls below the mean wind speed down to 0.82 m/s before rising back to its mean value. From Table 2, it can be observed that the extents in unsteady CP from the steady CP maximum are much shorter when the fluctuation amplitudes  $U_{\text{amp}}$  are reduced from  $\pm 76\%$  ( $\pm 2.60$  m/s) to  $\pm 39\%$  ( $\pm 4.26$  m/s). Hence, a significant (negative) drop in CP by 160% from the steady maximum CP at  $U_{\text{mean}} = 3.42$  m/s is observed as compared to 35% reduction at  $U_{\text{mean}} = 11.00$  m/s.

In the present study, periodically fluctuating wind conditions are detrimental to the VAWT model's CP due to the large  $U_{\text{amp}}$  fluctuations in wind speed at the sites. Kamau et al. [26,27] attributed the high amplitude fluctuations at the sites to the channeling effects of wind due to the many hills around the area with Garissa site depicting mixed diurnal variation for both day and night hours, while the Marsabit site showed enhanced nocturnal speeds. The authors applied empirical methods to analyze the wind energy potential at the two sites.

The empirical power densities at a height of 10 m were between 903–1119 W/m<sup>2</sup> and 37–97 W/m<sup>2</sup> for Marsabit and Garissa stations, respectively. From Equation (1), and based on the present study's VAWT model rotor swept area, this corresponds to wind power  $P_w$  of between 632–783 W for Marsabit site and 26–68 W for Garissa station.

The power law calculation, using Equation (2), obtained empirical wind power density of between 1776 W/m<sup>2</sup> and 2202 W/m<sup>2</sup> at a height of 50 m for Marsabit station [26]. However, in the interest of the present study, the numerical wind power was analyzed based on wind conditions measured at 10 m hub height.

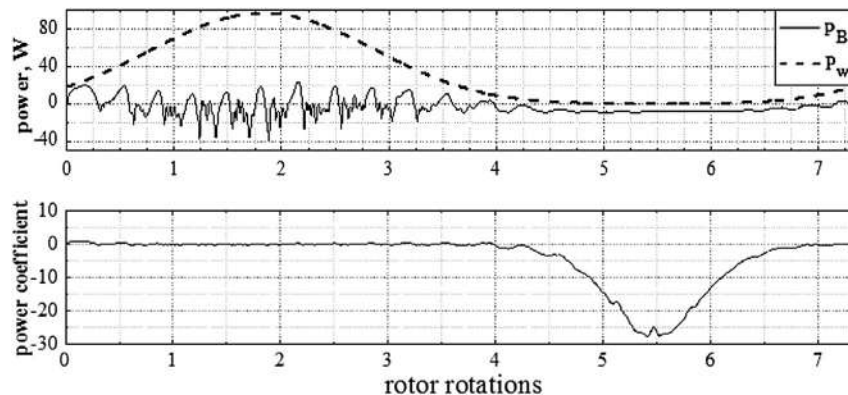


Fig. 13. One wind cycle  $P_B$ ,  $P_w$  and CP variations at 3.42 m/s.

**Table 3**  
Empirical and numerical wind power density.

Station	$U_{\text{mean}}$ (m/s)	$U_{\text{amp}}$ (m/s)	Power density ( $\text{W}/\text{m}^2$ )		Empirical power density ( $\text{W}/\text{m}^2$ )	
			Numerical	Empirical	Minimum	Maximum
Marsabit	11.00	4.26	997.76	1038	903	1119
Garissa	3.42	2.60	47.99	58	37	97

From Table 3, and using Equation (12), the numerical cycle averaged wind power per unit area (unsteady wind power density) is  $997.76 \text{ W}/\text{m}^2$  and  $47.99 \text{ W}/\text{m}^2$  for unsteady wind inflow at  $U_{\text{mean}}$  of  $11.00 \text{ m}/\text{s}$  and  $3.42 \text{ m}/\text{s}$ , respectively. The results falls within the minimum–maximum empirical power density range for both stations.

From the numerical results, Garissa site belongs to a wind class of  $\approx 1$ , while the Marsabit site with a high power density has a wind class  $> 7$ . The details about wind class can be obtained in Refs. [26,51]. That means, Garrissa site is unsuitable for grid-connected applications. This can be evidenced from the prolonged negative CP performance as can be observed in Fig. 13 and Table 2.

As can be seen in Fig. 12, the large positive CP performance registered at Marsabit makes the site suitable for grid-connected power generation. As shown in Table 3, the unsteady wind power density is observed to drop by 17% from the empirical power density (of  $58 \text{ W}/\text{m}^2$ ) for the largest fluctuation amplitude  $U_{\text{amp}}$  of  $\pm 76\%$  ( $\pm 2.60 \text{ m}/\text{s}$ ) at Garissa station. However, a marginal drop of 4% is observed for the lower fluctuation amplitude  $U_{\text{amp}}$  of  $\pm 39\%$  ( $\pm 4.26 \text{ m}/\text{s}$ ) at Marsabit station.

The numerical power performance results in Figs. 8–13 and Tables 2 and 3 are consistent to the previous studies in Danao et al. [5,22]. According to Danao et al. [5], unsteady CP fluctuates between different steady curves depending on the amplitude of the fluctuating wind. In their experimental study, two fluctuation amplitudes were considered, i.e.  $U_{\text{amp}} = \pm 12\%$  and  $U_{\text{amp}} = \pm 7\%$ . The overall cycle averaged CP was reduced when the VAWT was increased from  $U_{\text{amp}} = \pm 7\%$  to  $U_{\text{amp}} = \pm 12\%$ , for both mean tip speed ratios at  $\lambda_{\text{mean}} = 3.8$  and  $\lambda_{\text{mean}} = 4.1$ . Danao et al. [22] in their investigation run two simulations at  $U_{\text{amp}} = \pm 7\%$  ( $\pm 0.49 \text{ m}/\text{s}$ ) and  $U_{\text{amp}} = \pm 30\%$  ( $\pm 0.21 \text{ m}/\text{s}$ ), and compared to the reference case of  $U_{\text{amp}} = \pm 12\%$  ( $\pm 0.84 \text{ m}/\text{s}$ ) with 28 rotor cycles required to complete one wind cycle. Similar to the present study, the peaks of  $P_B$  followed the wind variation much like the  $T_b$  did. Moreover, a 24% drop in performance was observed for the largest fluctuation amplitude of  $U_{\text{amp}} = \pm 30\%$ , while a 6% improvement was seen for the smallest fluctuation amplitude at  $U_{\text{amp}} = \pm 7\%$ .

Scheurich and Brown [21], in their study to investigate the influence of fluctuation amplitude on a VAWT performance, also observed that the width of the  $\lambda$  range was wider for the  $U_{\text{amp}} = \pm 30\%$  case than the  $U_{\text{amp}} = \pm 10\%$  case. The fluctuating wind had a mean speed of  $5.4 \text{ m}/\text{s}$  with a fluctuation frequency of  $1 \text{ Hz}$ . The VAWT cycle averaged CP dropped to 92% of the ideal steady CP for  $U_{\text{amp}} = \pm 30\%$ , while a drop to 99% was registered for  $U_{\text{amp}} = \pm 10\%$ . In addition, Kooiman and Tullis [52] determined in their field tests that fluctuation amplitude has a linear effect on the performance of the VAWT where  $U_{\text{amp}} = \pm 15\%$  reduced performance by 3.6% from ideal wind conditions. The work by the authors show that, the overall performance degradation is observed when fluctuation amplitudes are high, while the frequency variation effect is minimal for the case of practical urban wind conditions under study.

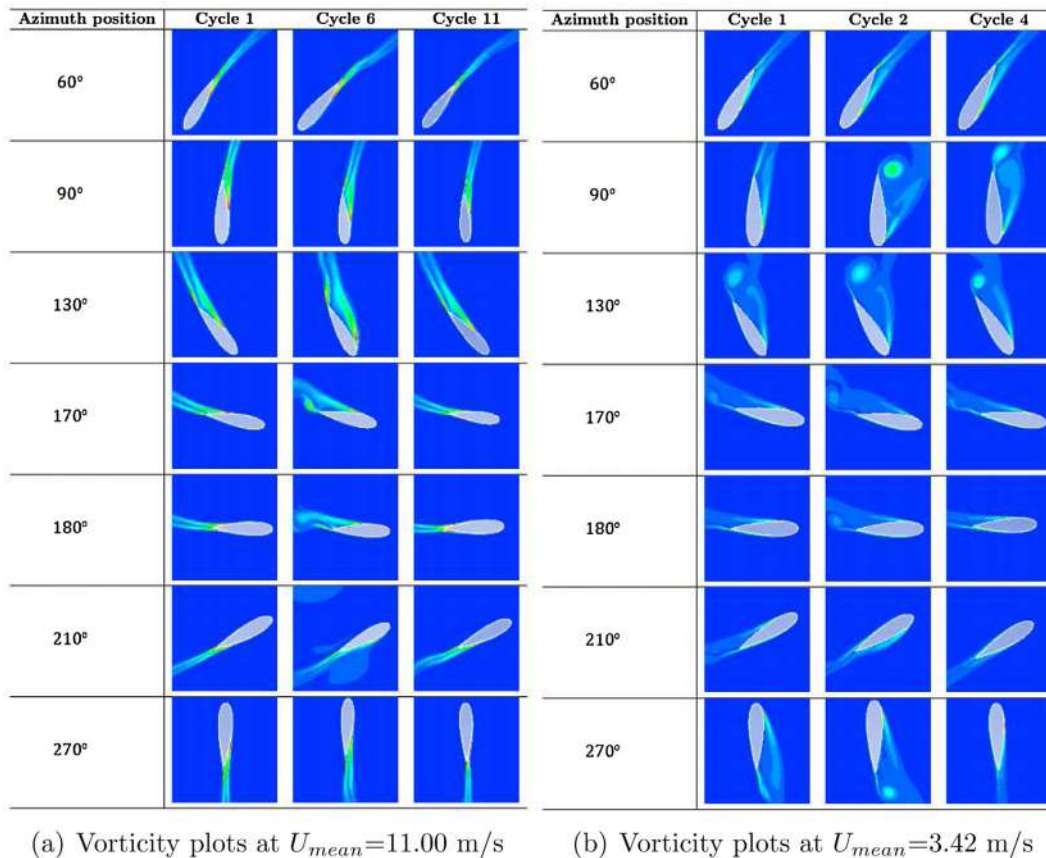


**Fig. 14.** Flow visualizations of vorticity profiles for three rotor cycles.

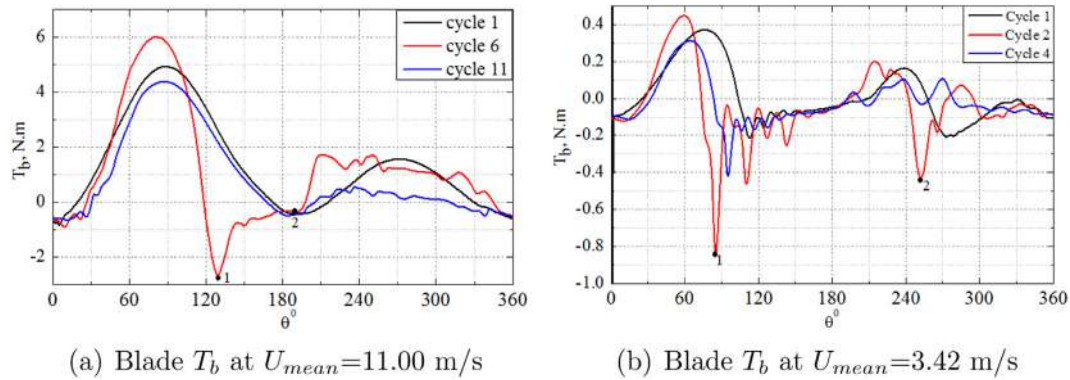


Fig. 15. Blade torques  $T_b$  across three rotor cycles.

#### 4.4. Flow visualization

Fig. 14(a, b) show flow visualization of vorticity profiles as the  $U_\infty$  fluctuates across the wind fluctuation cycle at  $U_{\text{mean}} = 11.00$  m/s and  $U_{\text{mean}} = 3.42$  m/s, respectively. Since there is no visible difference between the three blades at the same  $\theta$ , stalling of one blade at different rotor cycles is monitored. This could be the result of low frequency of the wind speed cycle compared to that of the rotor cycle [22,25].

From Fig. 14(a) it can be seen that there is no visible flow separation on the blade surface for azimuth position  $\theta = 60^\circ$  in all rotor cycles following thin wake. The region is associated with large positive torque as can be observed in Fig. 15(a). This is attributable to the stagnation point staying at the trailing edge.

Partial separation can be observed from  $\theta = 90^\circ$  in all rotations with visible full separation stall at  $\theta = 130^\circ$  in cycle 6 (refer to Fig. 14(a)). Fig. 15(a) shows that full separation can be associated with significant negative torque that the blade achieves in cycle 6 (Point 1). The large positive  $T_b$  values evident on the upwind side in Fig. 15(a) may be attributed to the unperturbed wind and  $\alpha$  near static stall that the blade experiences. A large negative drop in torque with full separated flow is visible at  $\theta = 130^\circ$  in cycle 6 extending to  $\theta = 170^\circ$  and even to  $\theta = 180^\circ$  (see Figs. 14(a) and 15(a)).

The vorticity flow field across both rotor cycles in the downwind region shows a similar pattern of re-attachment, and matches the blade torque plot (see Fig. 15(a)) from  $\theta = 210^\circ$  (Point 2) to  $\theta = 270^\circ$ . Beyond  $\theta = 270^\circ$ ,  $T_b$  drops in magnitude and blades start experiencing negative  $T_b$  fluctuation as they complete rotor cycle (see Fig. 15(a)). The large regions of negative torque and huge visible fluctuations in Fig. 15 agrees with deep stall and large flow separation of vortex shedding as shown in Fig. 14(a, b).

Observe in Fig. 15(a) that,  $T_b$  is largely positive throughout the upwind with notably high values produced from  $\theta = 60^\circ$  to  $\theta = 130^\circ$  for cycles 1 and 11, and between  $\theta = 60^\circ$  to  $\theta = 90^\circ$  for cycle 6. The stall within this azimuth range is relatively shallow, and only becomes significant after  $\theta = 130^\circ$ , where low torque is generated until the end of the upwind (Point 2). Generally, during upwind, the flow is attached to the surface for this wind condition.

In the downwind, re-attachment occurs immediately after  $\theta = 210^\circ$  for all cycles up to around  $\theta = 270^\circ$  due the low  $\alpha$  experienced by the blade surface. The high torque generated in the upwind leads to significant drop in the downwind flow velocity. As shown in Fig. 14(a), the blades experiences shallow stall, and negligible shedding of vortices in cycle 1 at  $U_{\text{mean}} = 11.00$  m/s.

From the vorticity plots in Fig. 14(b) at  $\theta = 60^\circ$  the separation bubble can be observed forming on the suction surface of the blade

in all the three rotor cycles at  $U_{\text{mean}} = 3.42$  m/s. It should be noted that  $U_{\text{mean}}$  of 3.42 m/s is the average wind speed for Garissa station with relatively high fluctuation amplitude of around  $U_{\text{amp}} = \pm 76\%$ . The negative torque performance is a consequence of very steep  $\alpha$  (see Fig. 7(c)) that the blade experiences at the regions inducing persistent large scale vortex shedding as evidenced in Fig. 14(b).

As can be seen in Fig. 15(b), the blade experiences significant drop in torque much earlier for cycle 2 than cycles 1 and 4 just before  $90^\circ$  (Point 1). This can be attributed to the deep stall on the blade surface as can be revealed by a visible separation bubble in cycle 2 (see Fig. 14(b)). At  $\theta = 90^\circ$  the separation bubble is observed to have developed into a dynamic vortex for both cycles 2 and 4, and already detached from the blade surface. In this region, the rotor cycles experience negative torque performance except for cycle 1 (see Fig. 15(b)). The vortex prediction is pronounced more clearly in all cycles as the blade approaches  $\theta = 130^\circ$  (see Fig. 14(b)).

In the downwind at  $\theta = 270^\circ$ , the observed visible separation bubble in cycle 2 can be associated with a significant drop in the blade torque as shown in Fig. 15(b) (Point 2). From Fig. 14(a, b), we may conclude that stall is more developed, and much deeper, on the blade surface in all rotor cycles at  $U_{\text{mean}} = 3.42$  m/s than at  $U_{\text{mean}} = 11.00$  m/s for the same azimuth position. As a result, the lower unsteady wind CP was recorded at Garrisa than Marsabit station because of the very large amplitude of fluctuation.

## 5. Conclusion

The unsteady inflow wind due to the rotation of the turbine operating in unsteady wind conditions has been introduced to investigate wind energy potential at Marsabit and Garissa, both towns in the Eastern region of Kenya. Numerical simulations using unsteady RANS based CFD method have been used to evaluate unsteady inflow wind performance at the sites and the results obtained compared to empirical method studies.

The numerical wind power  $P_w$  and blade power  $P_b$  cycle averages at Marsabit were 698.43 W and 204.86 W while at Garissa were 33.59 W and  $-4.30$  W, respectively. The computed unsteady wind CP was 0.30 at Marsabit and  $-0.13$  at Garrisa. The corresponding power density for Marsabit and Garissa was 997.76 W/m<sup>2</sup> and 47.99 W/m<sup>2</sup>, a marginal drop of 4% and 17% from the empirical results, respectively. The numerical results matches the empirical power density range from 903 W/m<sup>2</sup> to 1119 W/m<sup>2</sup> at Marsabit, and from 37 W/m<sup>2</sup> to 97 W/m<sup>2</sup> at Garissa station. The deterioration in performance at Garissa station was attributed to large  $U_{\text{amp}}$  fluctuations in wind speeds resulting to decrease in positive performance of the VAWT.

In addition, flow visualization of vorticity was also tested and compared to the wind performance using the CFD method as  $U_{\infty}$  fluctuated across the wind cycle. The large regions of negative wind performance and large visible fluctuations in wind speed were revealed by deep stall and large flow separation of vortex shedding. The findings lend substantially to our understanding of unsteady wind inflow performance, and the flow physics that affects the performance on VAWTs scale.

According to the numerical results, Garrissa station corresponds to wind class  $\approx 1$ ; hence, the site was found to be unsuitable for grid-connected power generation. However, Marsabit site with wind class  $>7$  was found to be suitable for grid-connected and stand-alone activities such as water pumping. As a result, the introduced CFD numerical method could be considered as an alternative, inexpensive and robust method for investigating wind power potential in both steady and unsteady winds. The results from the study will hopefully be of importance to the wind industries that require designs for wind turbines reflecting real unsteady wind environment.

### Acknowledgments

This research work was supported in part by the Institute of Dynamics and Control of Spacecrafts, of School of Astronautics, through Harbin Institute of Technology; and the Chinese Scholarship Council, through People's Republic of China Government (CSC No. 2013404003) in collaboration with the Kenyan Government.

### References

- [1] Singh RK, Ahmed MR, Zullah MA, Lee Y-H. Design of a low Reynolds number airfoil for small horizontal axis wind turbines. *Renew Energy* 2012;42(0): 66–76. <http://dx.doi.org/10.1016/j.renene.2011.09.014>.
- [2] Howell R, Qin N, Edwards J, Durrani N. Wind tunnel and numerical study of a small vertical axis wind turbine. *Renew Energy* 2010;35(2):412–22. <http://dx.doi.org/10.1016/j.renene.2009.07.025>.
- [3] Tai F-Z, Kang K-W, Jang M-H, Woo Y-J, Lee J-H. Study on the analysis method for the vertical-axis wind turbines having Darrieus blades. *Renew Energy* 2013;54(0):26–31. <http://dx.doi.org/10.1016/j.renene.2012.09.014>.
- [4] Islam M, Fartaj A, Cariveau R. Analysis of the design parameters related to a fixed-pitch straight-bladed vertical axis wind turbine. *Wind Eng* 2008;32(5): 491–507. <http://dx.doi.org/10.1260/030952408786411903>.
- [5] Danao LA, Eboibi O, Howell R. An experimental investigation into the influence of unsteady wind on the performance of a vertical axis wind turbine. *Appl Energy* 2013;107(0):403–11. <http://dx.doi.org/10.1016/j.apenergy.2013.02.012>.
- [6] Eriksson S, Bernhoff H, Leijon M. Evaluation of different turbine concepts for wind power. *Renew Sustain Energy Rev* 2008;12(5):1419–34. <http://dx.doi.org/10.1016/j.rser.2006.05.017>.
- [7] Eboibi O. The influence of blade chord on the aerodynamics and performance of vertical axis wind turbines. PhD Thesis. UK: The University of Sheffield; 2013. <http://etheses.whiterose.ac.uk/4730/>.
- [8] Roh S-C, Kang S-H. Effects of a blade profile, the Reynolds number, and the solidity on the performance of a straight bladed vertical axis wind turbine. *J Mech Sci Technol* 2013;27(11):3299–307. <http://dx.doi.org/10.1007/s12206-013-0852-x>.
- [9] Bedon G, Castelli MR, Benini E. Optimization of a Darrieus vertical-axis wind turbine using blade element momentum theory and evolutionary algorithm. *Renew Energy* 2013;59(0):184–92. <http://dx.doi.org/10.1016/j.renene.2013.03.023>.
- [10] Paraschivoiu I. Wind turbine design: with emphasis on Darrieus concept. ISBN 2-553-00931-3, Presses inter Polytechnique. 2002. p. 76. <http://books.google.com.hk>.
- [11] Raciti Castelli M, Benini E. Effect of blade inclination angle on a Darrieus wind turbine. *J Turbomach* 2012;134(3). <http://dx.doi.org/10.1115/1.4003212>.
- [12] Raciti Castelli M, Englaro A, Benini E. The Darrieus wind turbine: proposal for a new performance prediction model based on Cfd. *Energy* 2011;36(8): 4919–34. <http://dx.doi.org/10.1016/j.energy.2011.05.036>.
- [13] Consul C, Willden R, Ferrer E, McCulloch MD. Influence of solidity on the performance of a cross-flow turbine. In: 8th European wave and Tidal Energy Conference. Uppsala, Sweden; 2009. [www-civil.eng.ox.ac.uk](http://www-civil.eng.ox.ac.uk).
- [14] Eboibi O, Howell LADR, Edwards JM. A numerical study of the influence of blade profile and solidity on the performance of vertical axis wind turbines. In: 51st AIAA Aerospace Sciences Meeting including the New Horizons Forum and Aerospace Exposition; 2013. <http://dx.doi.org/10.2514/6.2013-1095>.
- [15] Sheldahl RE, Klimas PC. Aerodynamic characteristics of seven symmetrical airfoil sections through 180-degree angle of attack for use in aerodynamic analysis of vertical axis wind turbines. Tech. Rep. Albuquerque, NM (USA): Sandia National Labs; 1981. <http://dx.doi.org/10.2172/6548367>.
- [16] Viré A, Xiang J, Piggott M, Cotter C, Pain C. Towards the fully-coupled numerical modelling of floating wind turbines. *Energy Procedia* 2013;35:43–51. <http://dx.doi.org/10.1016/j.egypro.2013.07.157>.
- [17] Nobile R, Vahdati M, Barlow JF, Mewburn-Crook A. Unsteady flow simulation of a vertical axis augmented wind turbine: a two-dimensional study. *J Wind Eng Ind Aerodyn* 2014;125(0):168–79. <http://dx.doi.org/10.1016/j.jweia.2013.12.005>.
- [18] Saeidi D, Sedaghat A, Alamdari A, Alemrajabi AA. Aerodynamic design and economical evaluation of site specific small vertical axis wind turbines. *Appl Energy* 2012;101(0). <http://dx.doi.org/10.1016/j.apenergy.2012.07.047>.
- [19] McIntosh S, Babinsky H, Bertenyi T. Optimizing the energy output of vertical axis wind turbines for fluctuating wind conditions. In: 45th AIAA aerospace sciences meeting and exhibit, Reno, Nevada; 2007. <http://dx.doi.org/10.2514/6.2007-1368>.
- [20] McIntosh S, Babinsky H, Bertenyi T. Unsteady power output of vertical axis wind turbines operating within a fluctuating free-stream. In: 46th AIAA aerospace sciences meeting and exhibit, Reno, Nevada; 2008. <http://dx.doi.org/10.2514/6.2008-1324>.
- [21] Scheurich F, Brown RE. Modelling the aerodynamics of Vertical-axis wind turbines in unsteady wind conditions. *Wind Energy* 2013;16(1):91–107. <http://dx.doi.org/10.1002/we.532>.
- [22] Danao LA, Edwards J, Eboibi O, Howell R. A numerical investigation into the influence of unsteady wind on the performance and aerodynamics of a vertical axis wind turbine. *Appl Energy* 2014;116:111–24. <http://dx.doi.org/10.1016/j.apenergy.2013.11.045>.
- [23] Wekesa DW, Mutuku JN, Kamau JN. Microcontroller-based data logging instrumentation system for wind speed and direction measurements. *J Agric Sci Technol* 2012;14(1):176–89. <http://elearning.jkuat.ac.ke/journals/ojs/index.php/jagst/article/view/802>.
- [24] Wekesa DW, Wang C, Wei Y, Kamau JN. Wind resource assessment and numerical simulation for wind turbine airfoils. In: 15th International Workshop on Research and Education in Mechatronics (REM). El Gouna, Egypt. IEEE; 2014. p. 1–9. <http://dx.doi.org/10.1109/REM.2014.6920224>.
- [25] Wekesa DW, Wang C, Wei Y, Danao LA. Influence of operating conditions on unsteady wind performance of vertical axis wind turbines operating within a fluctuating free-stream: a numerical study. *J Wind Eng Ind Aerodyn* 2014;135(0):76–89. <http://dx.doi.org/10.1016/j.jweia.2014.10.016>.
- [26] Kamau JN, Kinyua R, Gathua JK. 6 years of wind data for Marsabit, Kenya average over 14 m/s at 100 m hub height; an analysis of the wind energy potential. *Renew Energy* 2010;35(6):1298–302. <http://dx.doi.org/10.1016/j.renene.2009.10.008>.
- [27] Kamau JN, Kinyua R, Gathua JK. An investigation of the utility scale wind energy for North-eastern Kenya region. *J Agric Sci Technol* 2012;13(2). <http://elearning.jkuat.ac.ke/journals/ojs/index.php/jagst/article/view/609>.
- [28] Zhang J, Chowdhury S, Messac A, Hodge B-M. Assessing long-term wind conditions by combining different measure-correlate-predict algorithms. In: ASME International Design Engineering Technical Conferences, Portland, Oregon; 2013. <http://dx.doi.org/10.1115/DETC2013-12695>.
- [29] Kumaraswamy BRY, Keshavan BG. Analysis of seasonal wind speed and wind power density distribution in Aimangala wind farm at Chitradurga Karnataka using two parameter Weibull distribution function. *Power Energy Soc General Meeting* 2011;1(4):24–9. <http://dx.doi.org/10.1109/PES.2011.6039587>. IEEE.
- [30] Cellura M, Cirrione G, Marvuglia A, Miraoui A. Wind speed spatial estimation for energy planning in Sicily: introduction and statistical analysis. *Renew Energy* 2008;33(6):1237–50. <http://dx.doi.org/10.1016/j.renene.2007.08.012>.
- [31] Lu L, Yang H, Burnett J. Investigation on wind power potential on Hong Kong Islands analysis of wind power and wind turbine characteristics. *Renew Energy* 2002;27(1):1–12. [http://dx.doi.org/10.1016/S0960-1481\(01\)00164-1](http://dx.doi.org/10.1016/S0960-1481(01)00164-1).
- [32] Danao LA, Qin N, Howell R. A numerical study of blade Thickness and camber effects on vertical Axis wind turbines. *Proc Inst Mech Eng Part A: J Power Energy* 2012;226(7):867–81. <http://dx.doi.org/10.1177/0957650912454403>.
- [33] Edwards JM, Danao LA, Howell RJ. Novel experimental power curve determination and computational methods for the performance analysis of vertical axis wind turbines. *J Sol Energy Eng* 2012;134(3):031008. <http://dx.doi.org/10.1115/1.4006196>.
- [34] McTavish S, Feszty D, Sankar T. Steady and rotating computational fluid dynamics simulations of a novel vertical Axis wind turbine for small-scale power generation. *Renew Energy* 2012;41(0):171–9. <http://dx.doi.org/10.1016/j.renene.2011.10.018>.
- [35] McIntosh S. Wind energy for the built environment, PhD Thesis. Cambridge: University of Cambridge; 2009. p. 105–6. <https://dl.dropboxusercontent.com>.
- [36] Raciti Castelli M, Dal Monte A, Quaresimin M, Benini E. Numerical evaluation of aerodynamic and inertial contributions to Darrieus wind turbine blade deformation. *Renew Energy* 2013;51(0):101–12. <http://dx.doi.org/10.1016/j.renene.2012.07.025>.
- [37] Goude A, Agren O. Simulations of a vertical axis turbine in a channel. *Renew Energy* 2014;63(0):477–85. <http://dx.doi.org/10.1016/j.renene.2013.09.038>.
- [38] Li C, Zhu S, Xu Y-L, Xiao Y. 2.5D large Eddy simulation of vertical axis wind turbine in consideration of high angle of attack flow. *Renew Energy* 2013;51(0):317–30. <http://dx.doi.org/10.1016/j.renene.2012.09.011>.

- [39] D'Alessandro V, Montelpare S, Ricci R, Secchiaroli A. Unsteady aerodynamics of a Savonius wind rotor: a new computational approach for the simulation of energy performance. *Energy* 2010;35(8):3349–63. <http://dx.doi.org/10.1016/j.energy.2010.04.021>.
- [40] Trivellato F, Castelli MR. On the Courant-Friedrichs-Lewy criterion of rotating grids in 2d vertical-axis wind turbine analysis. *Renew Energy* 2014;62(0):53–62. <http://dx.doi.org/10.1016/j.renene.2013.06.022>.
- [41] Tucker PG, Pan Z. Urans computations for a complex internal isothermal flow. *Comput Methods Appl Mech Eng* 2001;190(22–23):2893–907. [http://dx.doi.org/10.1016/S0045-7825\(00\)00266-8](http://dx.doi.org/10.1016/S0045-7825(00)00266-8).
- [42] Wang H, Wang J, Yao J, Yuan W, Cao L. Analysis on the aerodynamic performance of vertical axis wind turbine subjected to the change of wind velocity. *Procedia Eng* 2012;31(0):213–9. <http://dx.doi.org/10.1016/j.proeng.2012.01.1014>.
- [43] Wegner B, Maltsev A, Schnieder C, Sadiki A, Dreizler A, Janicka J. Assessment of unsteady (RANS) in predicting swirl flow instability based on (LES) and experiments. *Int J Heat Fluid Flow* 2004;25(3):528–36. <http://dx.doi.org/10.1016/j.ijheatfluidflow.2004.02.019>.
- [44] Wang S, Ingham DB, Ma L, Pourkashanian M, Tao Z. Numerical investigations on dynamic stall of low Reynolds number flow around oscillating airfoils. *Comput Fluids* 2010;39(9):1529–41. <http://dx.doi.org/10.1016/j.compfluid.2010.05.004>.
- [45] Rossetti A, Pavesi G. Comparison of different numerical approaches to the study of the H-darrieus turbines start-up. *Renew Energy* 2013;50(0):7–19. <http://dx.doi.org/10.1016/j.renene.2012.06.025>.
- [46] Hameed MS, Afaq SK. Design and analysis of a straight bladed vertical axis wind turbine blade using analytical and numerical techniques. *Ocean Eng* 2013;57(0):248–55. <http://dx.doi.org/10.1016/j.oceaneng.2012.09.007>.
- [47] Li Y, Calisal SM. Three-dimensional effects and arm effects on modeling a vertical axis tidal current turbine. *Renew Energy* 2010;35(10):2325–34. <http://dx.doi.org/10.1016/j.renene.2010.03.002>.
- [48] Vahdati M, Nobile R, Barlow J, Mewburn-Crook A. Dynamic stall for a vertical axis wind turbine in a two-dimensional study. *World Renew Energy Congr* 2011;15(0). <http://dx.doi.org/10.3384/ecp1>.
- [49] Sayed MA, Kandil HA, Shaltot A. Aerodynamic analysis of different wind-turbine-blade profiles using finite-volume method. *Energy Convers Manag* 2012;64(0):541–50. <http://dx.doi.org/10.1016/j.enconman.2012.05.030>.
- [50] Bertenyi T, Wickins C, McIntosh S. Enhanced energy capture through gust-tracking in the urban wind environment. In: 48th AIAA Aerospace Sciences Meeting including the New Horizons Forum and Aerospace Exposition; 2010. <http://dx.doi.org/10.2514/6.2010-1376>.
- [51] Bailey BH, McDonald SL, Bernardett DW, Markus MJ, Elsholz K. *Wind resource assessment handbook: fundamentals for conducting a successful monitoring program*. Tech. Rep. 14. Albany, NY (US): National Renewable Energy Lab., Golden, CO (US); AWS Scientific, Inc; 1997. DOI: NREL/SR-440-22223.
- [52] Kooiman S, Tullis S. Response of a vertical axis wind turbine to time varying wind conditions found within the urban environment. *Wind Eng* 2010;34(4):389–401 [accessed-5.10.14], <http://www.eng.mcmaster.ca>.